scientific reports

OPEN

Machine learning-driven design of wide-angle impedance matching structures for wide-angle scanning arrays

Sina Hasibi Taheri[1]✉, Javad Mohammadpour[1], Ali Lalbakhsh[1], Slawomir Koziel[2,3] & Stanislaw Szczepanski[2]

This paper introduces a versatile and efficient design methodology for optimizing wide-angle impedance matching (WAIM) configurations, enhancing the scanning range of arbitrary antenna arrays. The three-layered structure is modeled using the generalized scattering matrices (GSMs) of the layers, incorporating sufficient excited modes for efficient input impedance calculation. To broaden the method's applicability and meet manufacturing requirements, it also considers dielectric materials other than air between the array and WAIM. Machine learning (ML) algorithms are integrated to evaluate WAIM characteristics, reducing calculation time and resources while enhancing adaptability to new structures with minimal designer intervention. Decision Tree-based models are chosen to provide accurate prediction while minimizing the dataset preparation time. The methodology involves training a network using three ML algorithms, including decision tree, bagging, and random forest. Optimal WAIM parameters are efficiently determined using a genetic algorithm (GA). Three matching layers are designed and validated for several arrays operating at the frequency range between 9 and 11 GHz. The random forest model shows the best performance in predicting the WAIM behavior, with *RMSE*, R^2 scores, *MAPE* of 0.033, 0.916, and 2.161, respectively. Results demonstrate that the designed WAIMs effectively enhance the scanning range of both microstrip and waveguide arrays within the desired frequency range. The method achieves a calculation time of 0.3 s per angle, significantly faster than previous approaches, with a total runtime under an hour and minimal RAM usage (9.7 MB). This method offers an efficient framework for developing tools to design wide-angle scanning arrays and expand their applications.

Keywords Wide-angle impedance matching (WAIM), Machine learning (ML), Decision tree (DT) models, Generalized scattering matrix (GSM)

In Recent years, providing a high-gain and ubiquitous communication link has emerged as a prominent topic in telecommunication network applications. To address the issues, the proposed solutions typically involve high-gain beam-scanning antennas. In contrast to the preceding slow and heavy mechanically rotated alternatives, phased-array antennas (PAAs) offer reliable and agile beam-steering capabilities, making them ideal for modern applications such as communication-on-the-move. However, the primary challenge in developing a wide-angle phased-array antenna (WAPAA) is the limited scanning range of arrays, which is mostly restricted to $\pm 50^{\circ}$ in three radiation planes, including E-, D-, and H-planes[1,2]. This issue primarily arises from impedance variations of the array element at the extreme scanning angles. These variations are caused by rising mutual coupling level between the PAA's elements, leading to a dramatic drop in the antenna's delivered power, which hinders the achievement of wide-angle arrays[3]. Therefore, achieving a WAPAA requires complex electromagnetic (EM) manipulations. Numerous relevant studies have tackled this challenge to enhance the array's scanning range.

The first set of solutions addresses this issue by mitigating inter-element mutual coupling through modifications to the array's radiation structure[4–10]. Although mitigating mutual coupling reduces scanning loss

[1]School of Engineering, Macquarie University, Sydney, NSW 2109, Australia. [2]Department of Engineering, Engineering Optimization and Modeling Center, Reykjavik University, 102 Reykjavik, Iceland. [3]Faculty of Electronics, Telecommunications and Informatics, Gdansk University of Technology, 80-233 Gdansk, Poland. ✉email: sina.hasibitaheri@mq.edu.au

at extreme scanning angles, this approach requires complex redesigns of the array, limits the array's element choices, and increases the overall cost and complexity of the structure.

The second set of solutions involves placing wide-angle impedance matching (WAIM) superstrate above the aperture to compensate for impedance variation of the element at extreme scanning angles[11–23]. Earlier approaches included loading the waveguide array with multiple dielectric layers to create the necessary susceptance for impedance matching at those angles[11–13]. To achieve a consistent improvement across all radiation planes over a relatively large bandwidth, the dielectric slab was replaced with an engineered metamaterial layer, providing greater control over the impedance of the matching structure[13–19]. To minimize the need for designer expertise, several studies have focused on developing methodologies for designing the matching layer[20–23]. Initially, a method was proposed to design WAIMs for a dipole array by modeling the array-WAIM interaction as a set of uncoupled transmission lines[20]. Later, for analyzing large systems, a system-by-design (SbD) paradigm was deployed to design a matching structure that enhanced the waveguide array performance[21]. However, these two approaches were tailored to specific array elements and WAIMs, limiting the generalizability of the proposed approach. An element-independent design approach was proposed[22] to realize an anisotropic matching layer by optimizing the permittivity and permeability tensors. Similar to Ref.[20], their approach modeled the interaction between the array and the loaded layer using several uncoupled transmission lines. However, they incorporated the generalized scattering matrix (GSM) representation of the array element, making the approach independent of the element type. Viewing the matching layer as a metaradome, another element-independent design strategy was proposed[23] to protect the PAA performance from the detrimental effects of the nearby cover. Unlike Ref.[22], this method does not treat the metaradome as a homogeneous layer, allowing it to account for the complex interactions between the metaradome and the phased array antenna. This results in more accurate results, especially for non-homogenous structures. Furthermore, the metaradome was analyzed using a fast periodic method of moments (FPMoM) code, yielding high accuracy for planar periodic structures used as WAIM. However, the reliance on the FPMoM code limits the WAIM choice only to planar metamaterials, as the code's precision is primarily optimized for such configurations. Developing such a code for more complex structures requires extensive time and designer expertise, reducing the method's generalization and adaptability.

To address this issue, recent advances in machine learning (ML), particularly supervised learning techniques, have demonstrated significant potential to accelerate the prediction of EM behavior in complex structures without relying on intensive numerical codes[24–35]. Supervised ML models are trained on labeled datasets from a limited set of high-fidelity simulations, enabling them to learn the relationship between input parameters and output performance. These models then serve as surrogate models (SM), capable of generalizing performance predictions across a broader design space. This approach significantly reduces computational time and resource consumption while maintaining accuracy. Decision tree algorithms, a prominent category of supervised learning models, have been used in various applications such as antenna design[24–26], microwave medical sensing[27], intelligent surfaces[29], electromagnetic numerical modeling[30,31], and wireless propagation[32]. Previous studies have shown that tree-based models outperform well-known neural network-based learning methods, such as deep learning, when applied to tabular data, especially when only a limited amount of data is available. Leveraging the "wisdom of the crowd" theory, these models exhibit high data efficiency and require significantly less training data preparation time compared to deep learning approaches[35–41].

This paper presents a novel methodology for designing wide-angle impedance matching (WAIM) structures independently of the underlying array, offering several key contributions:

1. The proposed method significantly reduces computational cost and hardware requirements by focusing solely on analyzing the WAIM rather than jointly optimizing the array and the matching structure. This independent approach minimizes reliance on full-wave solvers while maintaining accuracy. Additionally, the methodology ensures precision by considering a sufficient number of excited modes and their interactions, leading to a more accurate characterization of WAIM performance.
2. A machine learning-based surrogate model is integrated to eliminate the need for complex numerical codes or computationally expensive full-wave solvers during optimization. The accuracy of the surrogate model is ensured through rigorous testing and comparison of different machine learning architectures, selecting the most reliable model for predicting WAIM characteristics. This enhances the accuracy of the design process, while maintaining computational efficiency.
3. The methodology accurately captures the interaction between the WAIM and the array, ensuring generalization across different array configurations. By incorporating the generalized scattering matrix (GSM) of the array into the calculations, the proposed approach enables WAIM designs that are adaptable to various array structures without requiring case-specific modifications.
4. The approach considers different practical fabrication constraints, extending the design methodology to non-planar WAIM structures. Unlike previous studies that assume an air gap between the WAIM and the array, this method incorporates the necessary support structures into the design. This allows for the development of more complex and practically realizable WAIM configurations that were previously constrained to planar geometries.

Methodology to design a wide-angle impedance-matching structure

Overview of the modular framework

This section outlines the proposed methodology for designing a matching structure to enhance power delivery at extreme scanning angles. Unlike integral equation-based approaches[42], our method adopts a modular perspective on the multi-layered configuration of the PAA, WAIM, and the intermediate layer, shown in Fig. 1. This modular approach allows for layer-by-layer modification, making the methodology adaptable and widely applicable.

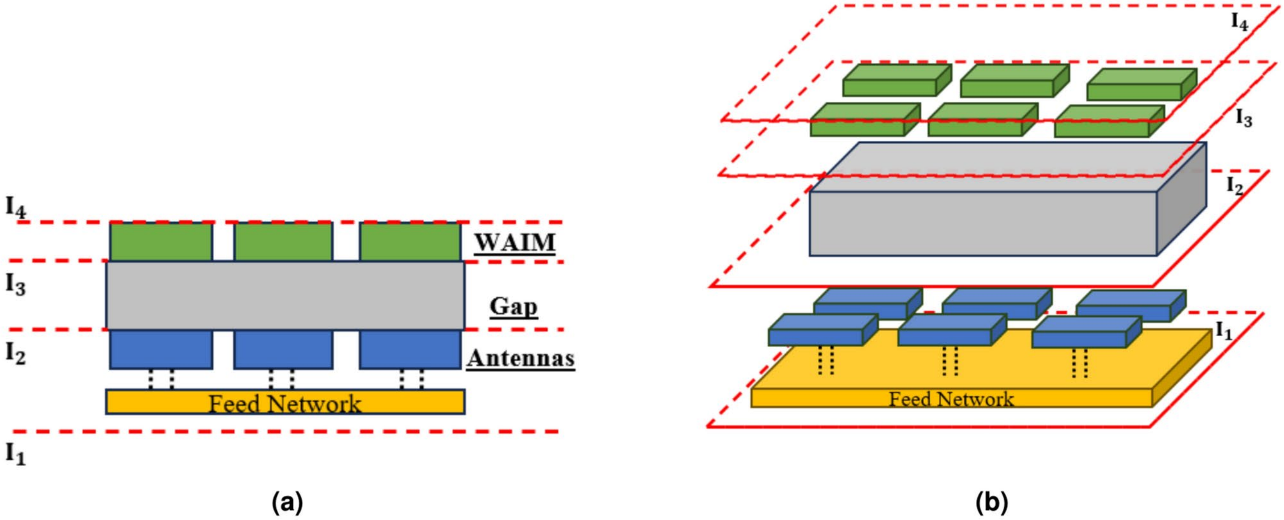

Fig. 1. (**a**) Example of the array with the WAIM and the gap between them. (**b**) Exploded view of the structure with the reference planes of each layer.

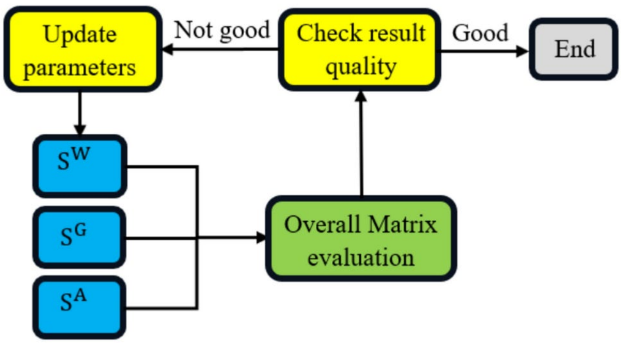

Fig. 2. Framework overview of the proposed method.

To provide an efficient and general method, the GSM concept is integrated to solve the problem. The framework, illustrated in Fig. 2, includes two main phases. The first phase involves calculating the loaded array matrix from its three constituent GSM matrices: S^A (antenna array), S^G (gap layer), and S^W (WAIM). The second phase focuses on preparing GSM data. By cascading the GSM and calculating the loaded array's input impedance, a global optimization procedure (yellow blocks) iteratively explores the WAIM parameters domain, adjusting each parameter to minimize the reflection coefficient and improve the overall impedance matching across the targeted scanning angles.

Overall GSM matrix formulation derivation

For a multi-layered periodic structure, based on the Floquet analysis[1], the fields at the intersections can be expressed as the superposition of a sufficient number of TE and TM modes. Due to the different characteristic impedances of excited modes, the GSM concept is used to represent the input–output relationship of each layer[43], normalizing each mode's incident and reflected waves to its characteristic impedance. Figure 3 illustrates the graphical visualization of the excited modes within the unit cell of the configuration. The large boxes represent each layer's GSM, with solid lines indicating forward and backward excited modes and dotted lines showing their connections at the intersections. In this model, it is assumed that m, n, and k modes (including both TE and TM modes) exist at I_2, I_3, and I_4 to construct the EM fields at each discontinuity. The number of required excited modes can be calculated from the desired accuracy, which is discussed briefly later. The antenna port at the I_1 plane can be excited by TEM or TE mode, depending on the antenna's feeding type. At I_4 (the boundary between the WAIM and free space), both propagating and evanescent modes exist. The evanescent modes can be assumed to be terminated with a loading impedance equal to their respective mode's impedance to model their non-traveling feature[20]. Hence, three GSMs with the size of $(m+1)(m+1)$, $(m+n)(m+n)$, $(n+k)(n+k)$ are formed for the S^A, S^G, and S^W, respectively. Connecting the identical modes at both sides of the intersections completes the loaded array model. The overall GSM of the three-layered structure is

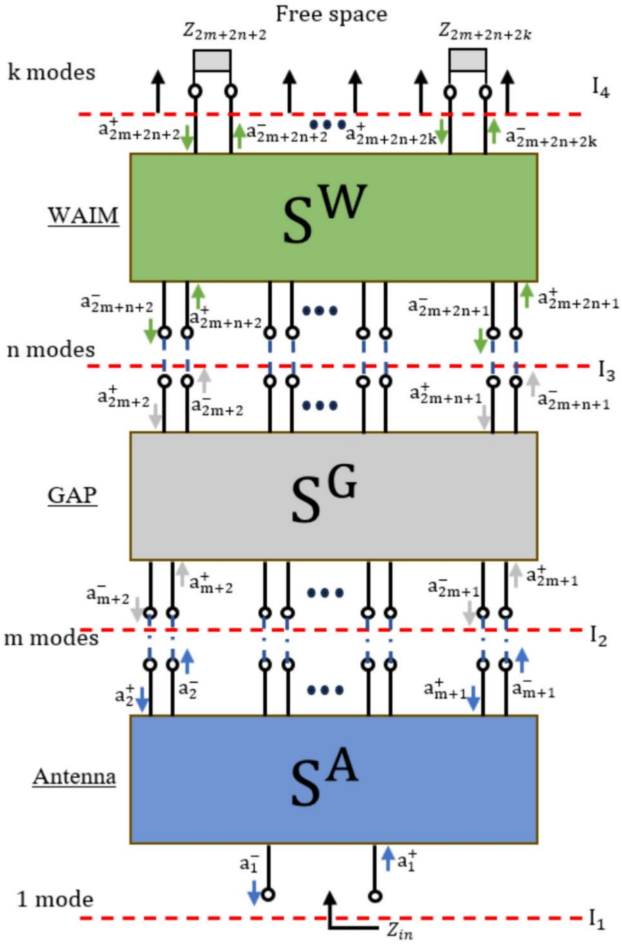

Fig. 3. Equivalent model for the loaded array formed by three cascaded GSMs.

then calculated by cascading the GSMs of the three layers[1,44]. Following the same procedure, the elements of the cascaded GSM, S^{AGW}, are defined as follows:

$$S_{11}^{AGW} = S_{11}^{A} + S_{12}^{A}\left(I - S_{11}^{GW} S_{22}^{A}\right)^{-1} S_{11}^{GW} S_{21}^{A} \tag{1a}$$

$$S_{12}^{AGW} = S_{12}^{A}\left(I - S_{11}^{GW} S_{22}^{A}\right)^{-1} S_{12}^{GW} \tag{1b}$$

$$S_{21}^{AGW} = S_{21}^{GW}\left(I - S_{22}^{A} S_{11}^{GW}\right)^{-1} S_{21}^{A} \tag{1c}$$

$$S_{22}^{AGW} = S_{22}^{GW} + S_{21}^{GW}\left(I - S_{22}^{A} S_{11}^{GW}\right)^{-1} S_{22}^{A} S_{12}^{GW} \tag{1d}$$

where I is the identity matrix. The elements of the S^{GW} can be calculated in the same way from the S^{W} and S^{G}.

It is worth noting that in the (1a–1d) each element of the three matrices is also a matrix. To identify them, first assume Eq. 2a represents the general form of a particular layer's GSM with M_1 modes on the input side and M_2 modes on the output side ($M_1 + M_2 = M$). Each $S_{ij}^{A,G,W}$ can then be defined as Eqs. (2b–2e).

$$S^{A,G,W} = \begin{bmatrix} S_{1,1} & \cdots & S_{1,M_1} & \cdots & S_{1,M} \\ \vdots & \ddots & \vdots & \ddots & \vdots \\ S_{M_1,1} & \cdots & S_{M_1,M_1} & \cdots & S_{M_1,M} \\ \vdots & \ddots & \vdots & \ddots & \vdots \\ S_{M,1} & \cdots & S_{M,M_1} & \cdots & S_{M,M} \end{bmatrix} \tag{2a}$$

$$S_{11}^{A,G,W} = \begin{bmatrix} S_{1,1} & \cdots & S_{1,M_1} \\ \vdots & \ddots & \vdots \\ S_{M_1,1} & \cdots & S_{M_1,M_1} \end{bmatrix}_{M_1 \times M_1} \tag{2b}$$

$$S_{12}^{A,G,W} = \begin{bmatrix} S_{1,M_1+1} & \cdots & S_{1,M} \\ \vdots & \ddots & \vdots \\ S_{M_1,1} & \cdots & S_{M_1,M} \end{bmatrix}_{M_1 \times M_2} \tag{2c}$$

$$S_{21}^{A,G,W} = \begin{bmatrix} S_{M_1+1,1} & \cdots & S_{1,M_1+1} \\ \vdots & \ddots & \vdots \\ S_{M,1} & \cdots & S_{M,M_1} \end{bmatrix}_{M_2 \times M_1} \tag{2d}$$

$$S_{22}^{A,G,W} = \begin{bmatrix} S_{M_1+1,M_1+1} & \cdots & S_{M_1+1,M} \\ \vdots & \ddots & \vdots \\ S_{M_1+1,M} & \cdots & S_{M,M} \end{bmatrix}_{M_2 \times M_2} \tag{2e}$$

As indicated in Eqs. (2b–2e), $S_{11}^{A,G,W}$ and $S_{22}^{A,G,W}$ represent the interactions between different modes in the input and output sides, respectively. $S_{12}^{A,G,W}$ and $S_{21}^{A,G,W}$ show the modal interaction between two sides of the layer. With the cascaded GSM, $S^{A,G,W}$, the input impedance of the loaded array can be calculated as[1]

$$Z_{\text{in}} = Z_{11} - Z_{12}\left(Z_L + Z_{22}\right)^{-1} Z_{21} \tag{3}$$

where Z_{ij} are the elements of the overall impedance matrix calculated using S^{AGW}, and Z_L is defined as follows[45]:

$$Z_L = \left(I + S_{11}^{\text{AGW}}\right)\left(I - S_{11}^{\text{AGW}}\right)^{-1} Z_0 \tag{4}$$

where Z_0 is the diagonal matrix, including the reference impedance of each mode on the input and output sides.

GSM preparation

As illustrated in Fig. 2, a key part of this methodology involves deriving the GSM for the three main components of the problem, S^A, S^G, and S^W, at different scanning angles (θ_i,ϕ_i). The following sections provide a detailed explanation of the extraction process for each layer's GSM.

(1) Array: Although there are analytical methods to derive the matrix for the simple elements, such as dipole and waveguide apertures[20,21], most array configurations require analysis using EM solvers. Although using an EM solver for the GSM evaluation can be time-consuming, this evaluation is performed once at the beginning of the design process and thus does not significantly impact the overall design time. Moreover, for infinite periodic PAAs, setting the parallel periodic boundaries of the array's unit cell allows for the evaluation of the unit cell only instead of the entire PAA, maintaining numerical accuracy and reducing calculation time.

(2) Gap layer: The same approach can be applied for the GSM extraction of the gap layer by EM solvers, which is particularly useful for complex support configurations that are difficult to model analytically. This method assumes that the gap layer is a simple dielectric material slab, allowing it to be modeled as several isolated transmission lines. This assumption is well-aligned with the conclusions in the Refs.[20,46] and imposes the same excited modes at two sides of the gap layer (m = n). Therefore, the elements of S^G can be derived as

$$S_{ij}^{(\mathrm{TE/TM})} = \begin{cases} \frac{\Gamma_i^{(\mathrm{TE/TM})} - \left(T_{12,i}^{(\mathrm{TE/TM})} T_{21,i}^{(\mathrm{TE/TM})} \Gamma_i^{(\mathrm{TE/TM})} e^{-j2\beta_i d}\right)}{1 - \left(\Gamma_i^{(\mathrm{TE/TM})} e^{-j\beta_i d}\right)^2} & \text{if} \quad i = j, \\ \frac{T_{12,i}^{(\mathrm{TE/TM})} T_{21,i}^{(\mathrm{TE/TM})} e^{-j\beta_i d}}{1 - \left(\Gamma_i^{(\mathrm{TE/TM})} e^{-j\beta_i d}\right)^2} & \text{if} \quad |i - j| = m, \\ 0 & \text{otherwise.} \end{cases} \tag{5}$$

(3) Matching layer: Previous studies have utilized EM commercial software[22] or numerical codes developed for specific configurations[23] to derive the WAIM's GSM. However, using commercial software in iterative procedures is time-consuming and inefficient. On the other hand, deploying numerical codes for specific structures reduces the computational time. However, in cases that new structures are utilized, a whole new code needs to be developed by the expert designers to predict the WAIM behavior. Supervised ML algorithms offer an alternative by creating surrogate models that approximate the EM behavior of the structures without needing expensive computational resources for iterative full-wave simulations or highly specialized numerical codes. SM training involves acquiring several datasets using a commercial EM solver. These training datasets include input–output pairs, where the input is WAIM geometric parameters, and the output is the corresponding GSM.

(3.1) SM training: The goal of training a surrogate model is to establish a mapping function between input and output datasets, (x_i,y_i), to emulate real-world behavior. The SM training procedure is illustrated in Fig. 4. Preparing the datasets requires understanding the WAIM performance. Using a commercial EM solver to simulate the WAIM, identified by the input vector x_i, the corresponding GSM is extracted to form y_i. In the "Data Split" section, the datasets are divided into training and testing datasets with a ratio of 4:1. The

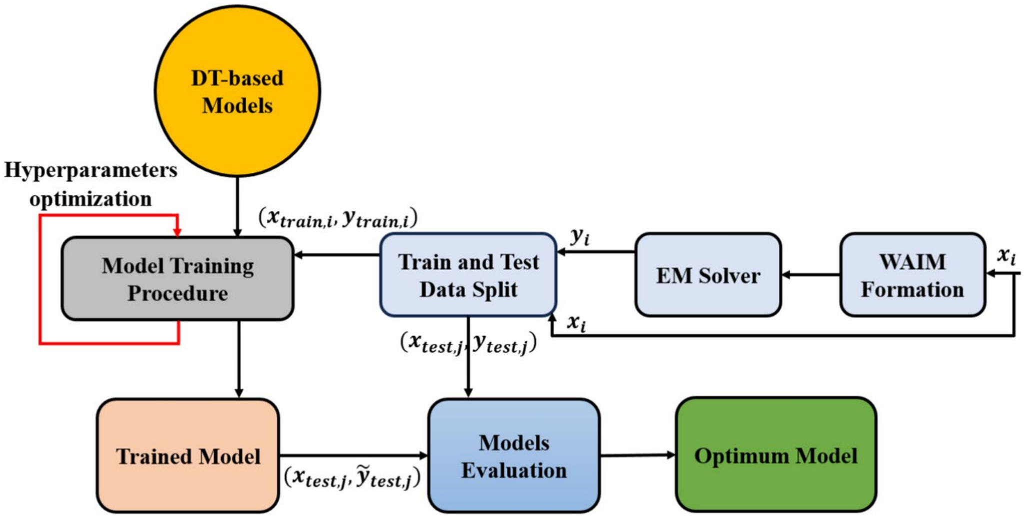

Fig. 4. Training procedure and selection of the best SM model.

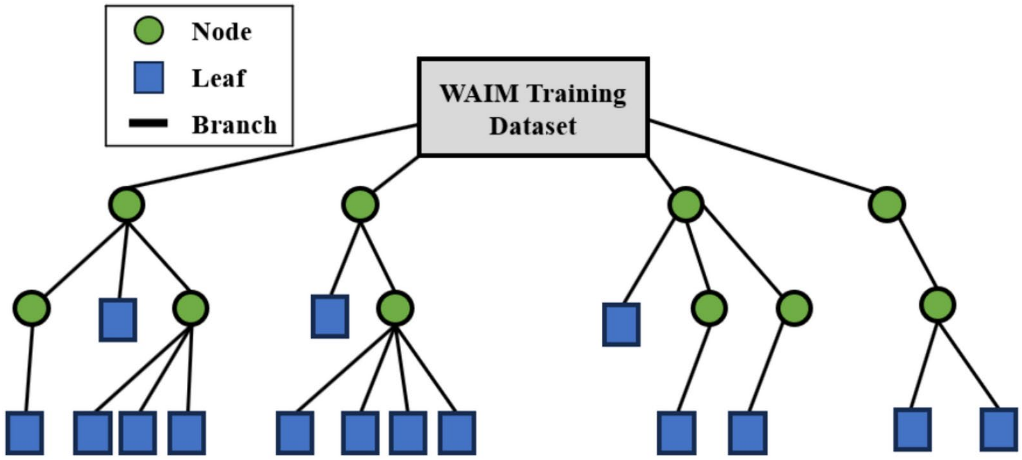

Fig. 5. Decision tree prediction structure.

training datasets are used to build a model based on a particular algorithm, with its hyperparameters optimized for the best performance. In the "Models Evaluation" block, the same procedure is repeated across multiple algorithms to identify the optimal model. The evaluation criteria for each trained model include mean root mean square error (*RMSE*), R^2 score, and mean absolute percentage error (*MAPE*) defined as follows:

$$RMSE = \sqrt{\frac{1}{N}\sum_{i=1}^{N} |y_i - \tilde{y}_i|^2} \tag{6a}$$

$$R^2 = \frac{\sum_{i=1}^{N} |y_i - \tilde{y}_i|^2}{\sum_{i=1}^{N} |y_i - \bar{y}|^2} \tag{6b}$$

$$\mathrm{MAPE} = \frac{1}{N}\sum_{i=1}^{N} \left|\frac{y_i - \tilde{y}_i}{y_i}\right| \times 100 \tag{6c}$$

where y_i is the actual value, $\tilde{y}_i$ is the predicted value, and $\bar{y}$ is the mean of the actual values for training and testing outputs. In this study, three widely used ML algorithms based on decision tree models are selected as follows

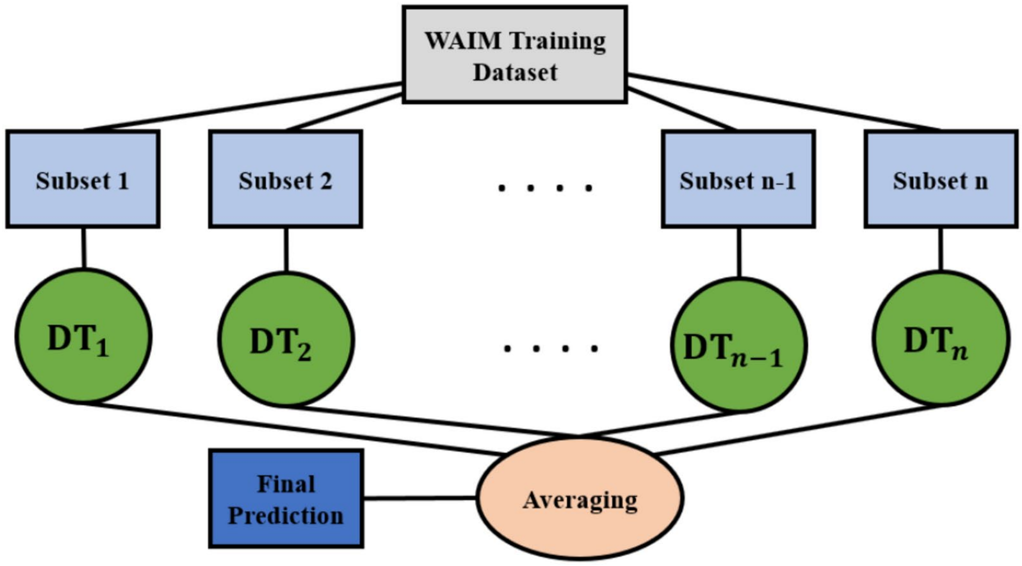

Fig. 6. Bagging method prediction structure.

- Decision tree

The Decision Tree (DT) model starts training at the root, where the most significant feature for making predictions is chosen. The tree then grows by splitting nodes based on this feature to minimize error, continuing until a stopping criterion, such as a maximum depth or minimum node size. Figure 5 shows the structure of the decision tree algorithm. In this tree-like structure, each internal node represents a test on a feature, each branch represents the outcome of the test, and each leaf node represents the final prediction.

- Bagging

Bootstrap Aggregating, or bagging, is an ensemble learning method, illustrated in Fig. 6. In bootstrapping, multiple new random subsets are created from initial training datasets, allowing each dataset to be selected more than once. For each subset, DT is trained, and the final prediction results from aggregating all the DT's outputs. Training with random subsets enhances the model's robustness for data variations.

- Random forest

As an extension of the bagging method, the Random Forest (RF) algorithm creates subsets by bootstrapping data and training each DT with a random subset of features. The random feature selection at each split ensures diverse decision nodes and reduces the correlation between trees, resulting in more robust predictions. After training a forest of DTs, the model's final decision is the average of individual tree predictions. Unlike bagging, which uses all features for each tree, RF limits the features at each split, creating a unique and less correlated ensemble.

Optimization procedure

In this study, optimization aims to navigate the design procedure within a defined solution space and evaluate each step to get as close as possible to the global optimum. As shown in Fig. 2, the optimization process includes two main parts: calculating the cost function to assess the quality of each point and making decisions to determine the next step in the optimization path. This process continues until the stopping criterion is met.

Designing procedure

The procedure for designing the matching structure involves using an iterative optimization technique to determine the optimal geometric parameters. This approach compensates for impedance mismatches in the cascaded structure at specific scanning angles and frequencies. Figure 7 illustrates the design procedure for the matching structure. The blue blocks indicate the inputs, the grey ones represent the processes, and the output, containing optimal parameters, is the green block. The procedure starts with acquiring the GSM for the array and the intermediate layer. Using the array's GSM, a suitable shape for the matching structure is determined to compensate for impedance mismatches. The next step involves defining the solution space, crucial for training the ML algorithm and the optimization procedure. The boundaries of this solution space are often specified by the limitations imposed on the matching layer parameters and other design constraints. This space can be multidimensional, with each point representing a unique set of parameters that meet the problem's constraints. Each set of parameters corresponds to a specific matching layer configuration. By forming the WAIM using these parameters, S^W is evaluated by the well-trained DT-based model. With all three matrices in hand, the cascaded matrix is calculated at each frequency and direction. Subsequently, the loaded array's input impedance

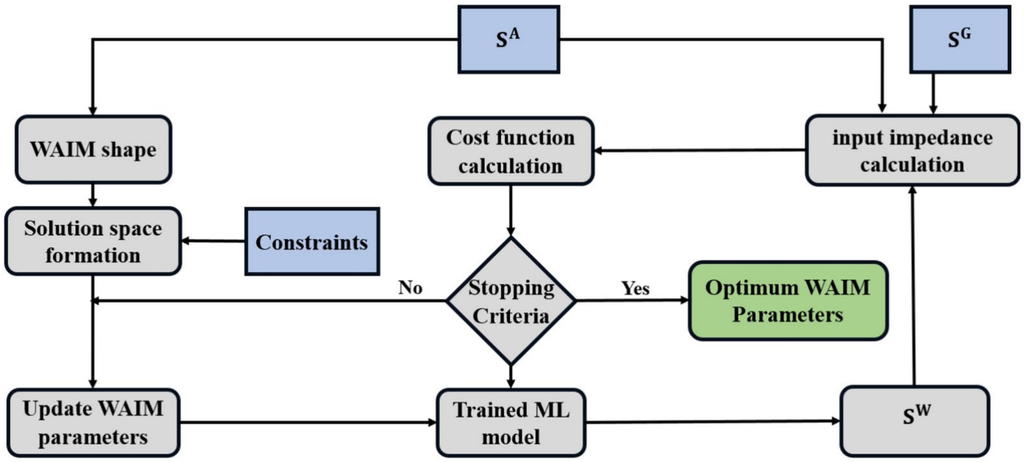

Fig. 7. Flowchart of the methodology.

and the corresponding reflection coefficient are evaluated from the acquired equivalent matrix. To evaluate the quality of the result, a cost function is defined as follows:

$$\sum_{f}\sum_{\theta}\sum_{\phi} w(f,\theta,\phi)\,|\Gamma(f,\theta,\phi,\epsilon,d)|^2 \tag{7}$$

where ϵ and d are the permittivity and the height of the gap layer, respectively. The weighting function (w) is defined by the difference between calculated (Γ_{dB}) and the desired reflection coefficient ($\Gamma_{desired}$) for each unmatched set of (f,θ,ϕ) as defined below:

$$w(f,\theta,\phi) = \begin{cases} 0 & \text{matched condition} \\ |\Gamma_{\mathrm{dB}}| - |\Gamma_{\mathrm{desired}}| & \text{unmatched condition} \end{cases} \tag{8}$$

Unlike the traditional cost functions that rely on averaging strategies, adaptive methods adjust the weights of the suboptimal reflection coefficients to avoid local minima[21,23]. By defining the cost function, the optimization can systematically explore the solution space, evaluate each iteration, and adjust parameters to converge on the optimal matching structure configuration. To improve accuracy, it is important to evaluate a number of excited modes, as shown in Ref.[1]. To achieve 95% dissipation of the highest-order evanescent mode beneath the WAIM interface, the number of highest-order can be calculated using Eq. 9.

$$M = \frac{2D_x D_y}{d^2} \tag{9}$$

where M shows the highest excited mode number, D_x and D_y are the unit-cell dimensions, and d is the height of the gap layer.

Examples and results

In this section, three designs based on the methodology are presented, demonstrating the method's potential to improve the array's scanning range. All examples utilize 3D structures instead of conventional 2D surfaces to highlight the capabilities of 3D structures in reducing the array's scanning loss. In contrast to 2D surfaces, 3D structures feature variations in the direction of EM wave propagation. The first two examples use a U-slot microstrip antenna as the element of array. The first one assumes air as the intermediate layer, while the second one highlights the capability of the methodology in taking into account the effects of the gap layer dielectric constant. To demonstrate the versatility of the proposed method in designing for different array structures, the third example investigates a circular waveguide array and presents a design aimed at enhancing its radiation performance.

U-slot patch with air gap

In this example, a U-slot patch antenna is used as the array element. The unit cell is designed at 10 GHz and illustrated in Fig. 8. The array has a square lattice with a 14 mm period, less than half of the wavelength, to prevent grating lobes. The radiating part is printed on a Rogers RT Duroid 5880 laminate with a thickness of 3.175 mm. Figure 9 shows the color-coded graphs of the array's active VSWR across various frequencies and scanning angles within three principal planes (E, D, and H), spanning 9–10.25 GHz. The initial contour signifies a VSWR of 2, denoting a matched impedance, while subsequent contours represent VSWR values of 4 and 6. The array demonstrates a scanning range of approximately 35° within the selected bandwidth across all planes. The design goal is to extend the scanning range to 70° between 9 and 10.25 GHz (13% fractional bandwidth) across

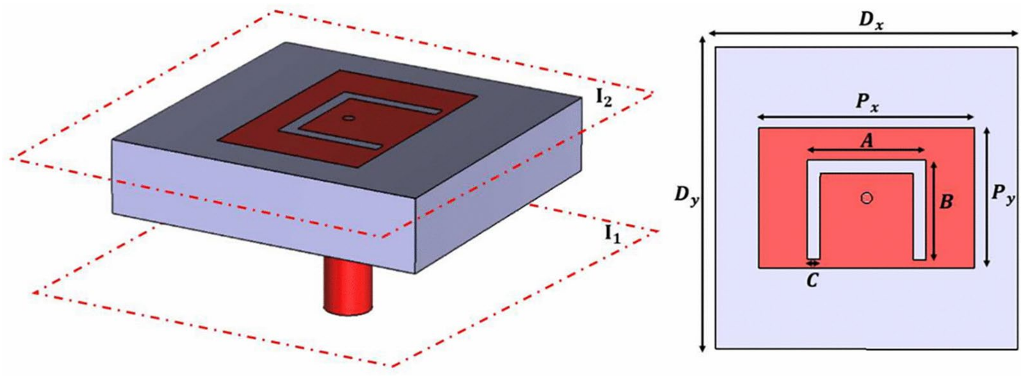

Fig. 8. Perspective and top view of the coaxial-fed U-slot.

three principal planes. In the first design, air is used as the material of the intermediate layer. According to Fig. 7, the initial step is to provide the inputs (GSMs for the array's element and the gap layer).

Based on Eq. 9, 25 modes are applied to ensure accurate calculations. The next step involves defining the configuration of the matching structure. The shape needs to offer the compensatory impedance required for matched conditions. Observing the frequency behavior of the array's impedance at extreme angles, shown in Fig. 10a, illustrates that a significant part of the unmatched impedance has capacitive behavior. To provide the necessary inductive impedance, one option is to place a set of two vertical metallic slabs above the array[18,47]. Figure 10b illustrates the configuration of the two metallic strips, designed to provide the required impedance for all three planes.

Knowing the WAIM's shape, the solution space boundaries are defined based on the problem's constraints. We restrict the height of each slab to a quarter wavelength to maintain a low-profile structure. In addition, the overall width of the WAIM should not exceed the unit cell size. Table 1 shows the variation range of the WAIM geometrical parameters to produce the desirable impedance at the desired frequencies. This solution space is utilized to prepare datasets required for training the ML models to predict the WAIM's characteristics. The solution space is utilized to prepare the dataset for training the ML models to predict the WAIM's characteristics. A total of 160 training data points is used to cover the input space, and 40 test data points are chosen to effectively evaluate the model's predictive ability under unseen conditions. The input vector includes the structure's geometrical variables and scanning angles, $x_i = [w_x, w_y, g_x, g_y, l_x, l_y, h_x, \theta_i, \phi_i]$. The corresponding WAIM's GSM, extracted from EM simulation, serves as the output, comprising extracted GSM at 21 equally spaced frequencies between 9 and 11 GHz.

To achieve an accurate model, three algorithms, including DT, bagging, and RF, are trained using the same training datasets. After training and tuning the corresponding hyperparameters, the model with the least prediction error is selected to act as a surrogate for the EM solver, as shown in Fig. 4. Table 2 shows the corresponding evaluation metrics, *RMSE*, R^2, and *MAPE* score for each method.

The RF model yielding the minimum prediction error is selected as the WAIM characteristic predictor at the frequency range between 9 and 11 GHz. Table 3 outlines the range of hyperparameters for each ML model, with the selected values highlighted in bold.

By calculating the loaded array's input impedance and the reflection coefficient to assess the quality of WAIM configuration on improving the overall array's condition, the cost function is calculated at eleven equally spaced frequency samples between 9 and 10.25 GHz, and eight observation angles ($\theta = 0$, 30, 45, 55, 60, 65, 70, 75) in three radiation planes, resulting in 24 observing angles in total. These observation angles match those used for training the SM. The distance between different observation angles is determined based on the extreme variation of angular behavior in the array's impedance response at large scanning angles. The design goal is set to maintain the VSWR below two at each observation angle and across all frequencies, setting $|\Gamma_{desired}|$ in Eq. 8 to -10 dB.

A genetic algorithm is used as the final step to optimize the WAIM parameters. After 350 generations, GA meets its termination criteria, and the optimal parameters for the metallic strips are identified. The full-wave simulated VSWR results, shown in Fig. 11, illustrate the matching condition of the loaded array. The expansion of the region covered by the first contour (VSWR equal to 2) compared to Fig. 9 shows that the scanning range reaches 70° for all three planes, achieved within 13% of bandwidth. As can be seen, the results exceed the target by 5° in two planes, providing impedance matching up to 70° on all three planes. Table 4 presents the parameters of the designed array.

Figure 12 compares the broadside and extreme scanning angles performance calculated by our method with the full-wave simulations. The circles show the calculated VSWR, while the lines represent the full-wave results. The excellent agreement with the simulated results indicates that the SM is well-trained and accurately predicts the WAIM characteristics. A key factor contributing to the model's accuracy is its consideration of modal interactions within the WAIM structure, unlike methods in Refs.[20,22], which assumed excited modes as isolated transmission lines. Figure 13 highlights this by comparing the full-wave simulated results with the VSWR calculated from both methods. Considerable discrepancies can arise when modal interactions are not considered, highlighting the importance of including higher mode interactions in the calculations, as their coupling levels are no longer negligible.

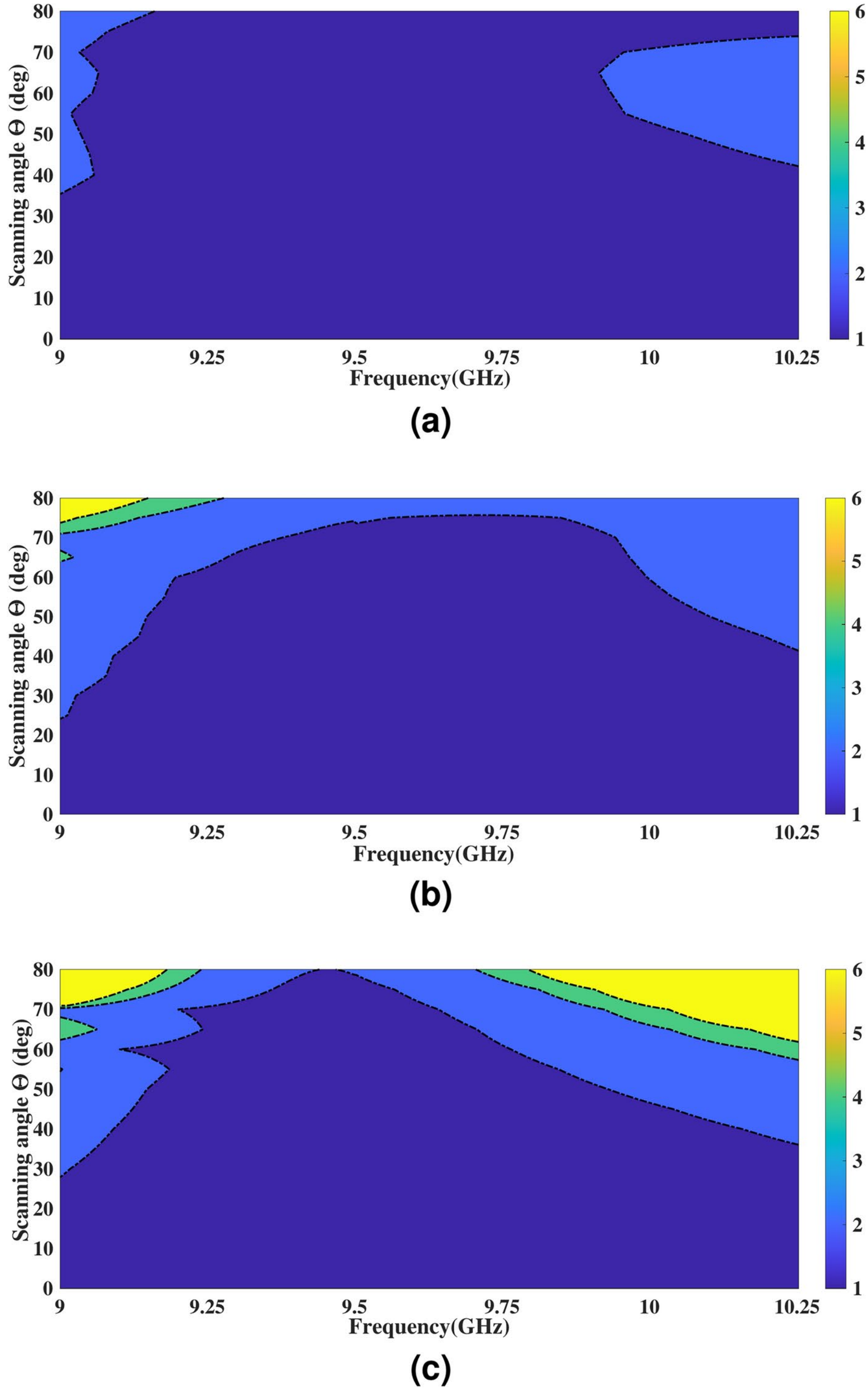

Fig. 9. VSWR representation of unit cell element as a function beam scanning direction and frequency in the desired bandwidth at (**a**) E-plane, (**b**) D-plane, (**c**) H-plane. The area surrounded by the first contour shows VSWR less than 2.

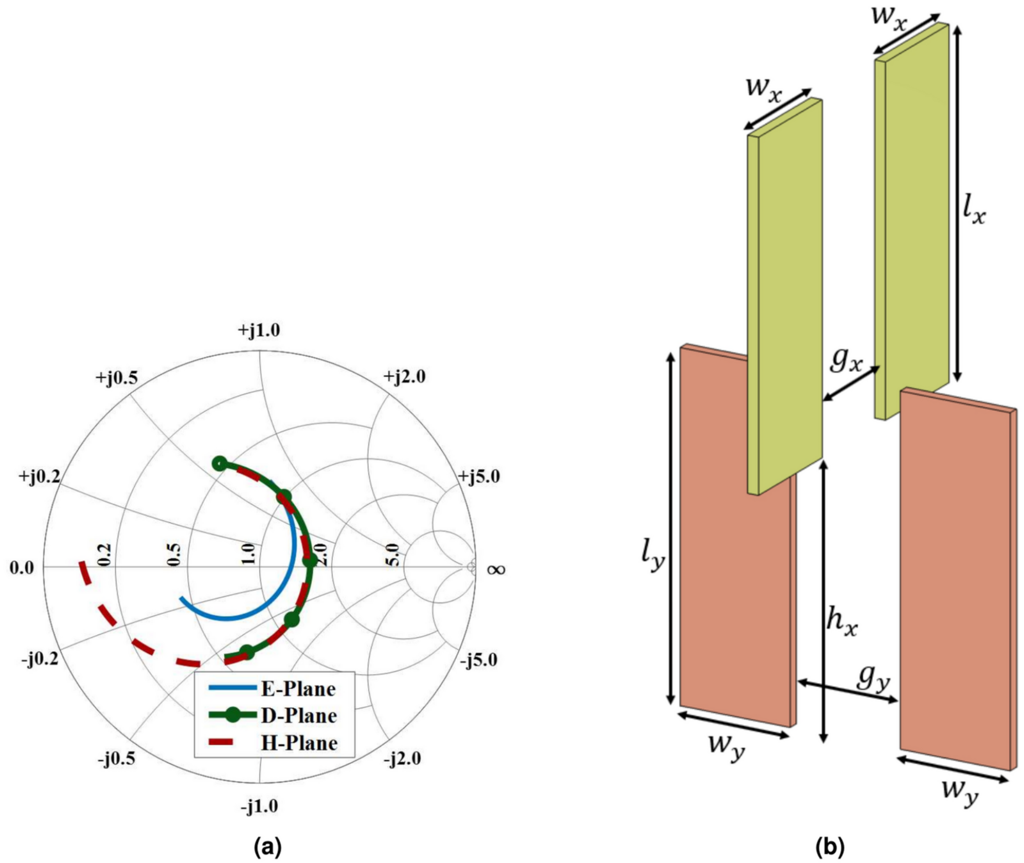

Fig. 10. (**a**) Smith Chart representation of array at extreme angles between 9 and 10.25 GHz. (**b**) Configuration to compensate the impedance mismatch.

Geometrical variables	Training data (160 samples)			Testing data (40 samples)		
	Min	Max	Step	Min	Max	Step
w_x, w_y	1.00	5.00	0.5	1.25	5.25	0.5
g_x, g_y	1.00	4.00	0.5	1.25	4.25	0.5
l_x, l_y	1.00	7.50	0.5	1.25	7.25	0.5
h_x	0.00	7.00	1.0	0.50	7.50	1.0

Table 1. Training and testing data range.

	DT			Bagging			RF		
	RMSE	R^2	MAPE	RMSE	R^2	MAPE	RMSE	R^2	MAPE
Training	0.014	0.990	0.922	0.020	0.977	1.626	0.009	0.995	0.787
Testing	0.061	0.782	3.745	0.042	0.824	3.279	0.033	0.916	2.161
Training time (s)		95.06			547.71			1120.24	

Table 2. Evaluation metrics corresponding to the three networks.

ML model	Hyperparameter	Range
DT	max_leaf_nodes	[100, 200, **500**, 1000]
	max_depth	[20, **30**, 50, 100]
	max_features	[0.5, 1, 2, 4, **8**]
Bagging	n_estimators	[20, **50**, 100, 200]
	max_depth	[20, **30**, 50, 100]
	max_features	[0.5, 1, 2, 4, **8**]
RF	n_estimators	[20, **50**, 100, 200]
	max_depth	[20, 30, **50**, 100]
	max_features	[0.5, 1, 4, **8**]

Table 3. Model's hyperparameter ranges.

To demonstrate the improvement in the delivered power to free space, the co-polarized component of the array's realized gain is analyzed[1] as follows:

$$G(\theta,\phi)=\frac{4\pi A\cos\theta}{\lambda^2}\left|S_{21}^{TE}(\theta,\phi)\sin\phi+S_{21}^{TM}(\theta,\phi)\cos\phi\right|^2 \tag{10}$$

Figure 14 illustrates the relative gain improvement as a function of scanning angle for different frequencies, indicating enhanced power transfer with the WAIM. The addition of the matching structure improves the array's delivered power, particularly at extreme angles, across the desired bandwidth without compromising the broadside performance.

Table 5 presents a detailed performance comparison with other relevant works to validate our methodology. Although this matching has a higher profile compared to traditional 2D surfaces, its significant achievements in scanning angles, bandwidth, and gain improvements at extreme scanning angles highlight the potential of 3D structures for WAIM design.

U-slot patch with the gap filled with dielectric

The second example assumes a dielectric layer between the array and the WAIM. This setup demonstrates the methodology's capability to analyze the intermediate layer and highlights the advantage of deploying ML models to design the same WAIM configuration for various array structures. Using the same design setting as the previous example, the dielectric permittivity of the gap layer is set to 2.2. In the previous example, a model was trained to predict the WAIM behavior over the band of interest 9–11 GHz. This model is now used to evaluate the WAIM, eliminating the need for additional dataset preparation. The GA meets the stopping criterion after passing 260 generations of calculations. The full-wave simulation of the resultant structure's VSWR is shown in Fig. 15. In this figure, the first two contour values represent the VSWR equal to 2 and 4, respectively. As indicated, the scanning range is improved to 70° over the desired frequency range.

Table 6 lists the parameters of the designed array. For validation, Fig. 16 compares the simulated results from the HFSS (shown as solid lines) with the VSWR predicted by our method (represented by circles of the same colors). The excellent agreement between both results demonstrates that this methodology effectively considers the effects of the gap layer in the design process. This capability is particularly valuable in designing a supporting structure for the complex WAIM structures, addressing one of the challenges associated with using matching layers to enhance the scanning range of arrays. The relative gain improvement as a function of scanning angle for different frequencies is shown in Fig. 17, indicating enhanced power transfer by adding the WAIM structure.

Circular waveguide with air gap

The third experiment explores the application of the proposed methodology to waveguide arrays, demonstrating its generality in designing matching structures for different array element configurations. This design aims to improve the scanning range of the waveguide array at the frequency range between 9 and 11 GHz. The radiating element in this configuration is a circular waveguide with a radius of 6.2 mm, filled with a dielectric with permittivity of 2.54[21]. The unit cell of the waveguide antenna is shown in Fig. 18. Here, the array lattice is a 14×14 square to prevent the grating lobe in the desired scanning range. To achieve the GSM of the circular waveguide, the unit cell is simulated at multiple scanning angles across three principal planes. The simulated VSWR values are presented in Fig. 19, illustrating that the waveguide is unmatched throughout the entire scanning range across different frequencies.

To further demonstrate the effectiveness of the 3D matching structure used in the previous examples, the same configuration, as shown in Fig. 10b is utilized to enhance the impedance matching condition. Utilizing the simulated GSM of the array obtained from the commercial software and the trained ML model for the WAIM structure from the previous cases, the optimization successfully converged after 290 generations. The parameters of the WAIM structure are detailed in Table 7.

To evaluate the improvement in the scanning performance of the array, the designed structure was simulated, and the VSWR results for the three principal radiation planes are presented at Fig. 20. The expansion of the first contour coverage, indicated in dark blue, across all scanning angles within the desired frequency range

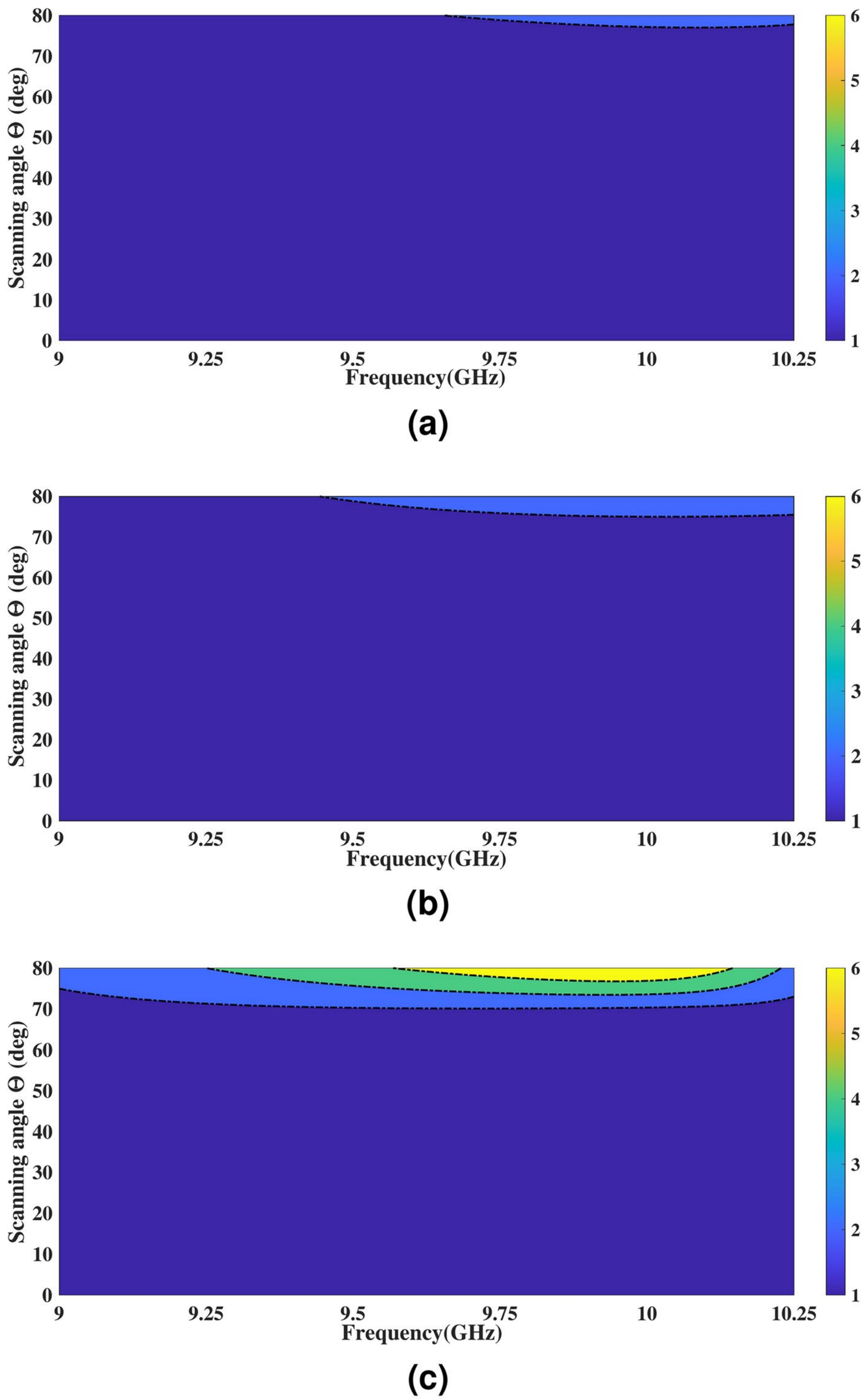

Fig. 11. VSWR of full-wave simulation of the unit cell of loaded structure as a function beam scanning direction and frequency in the desired bandwidth at (**a**) E-plane, (**b**) D-plane, (**c**) H-plane. First contour shows VSWR less than 2.

(particularly between 9.5 and 10.5 GHz) demonstrates the scanning range enhancement of the waveguide array. This improvement is achieved through the loaded matching structure, designed using the proposed methodology.

Another way to demonstrate the radiation enhancement of the loaded array is by comparing the gain performance in both cases: with and without WAIM. This comparison is illustrated in Fig. 21. As shown, improving the impedance matching of the array leads to a significant gain enhancement particularly at extreme angles. In these angles, the gain increases by approximately 5 dB across different radiation planes. This result

Variable	Value (mm)	Variable	Value (mm)	Variable	Value (mm)	Variable	Value (mm)
w_x	2.9	l_x	7.4	D_x	14	A	5.5
w_y	4.4	l_y	4.1	D_y	14	B	4.6
g_x	1.8	h_x	5.2	P_x	10	C	0.6
g_y	1.9	d	4.5	P_y	6.5		

Table 4. Dimensions of designed loaded array.

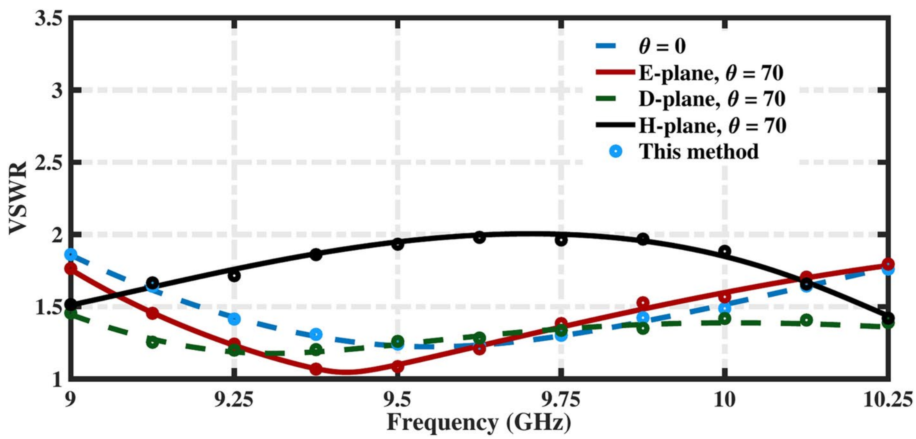

Fig. 12. Comparison between the outcome of proposed method and full-wave simulation results.

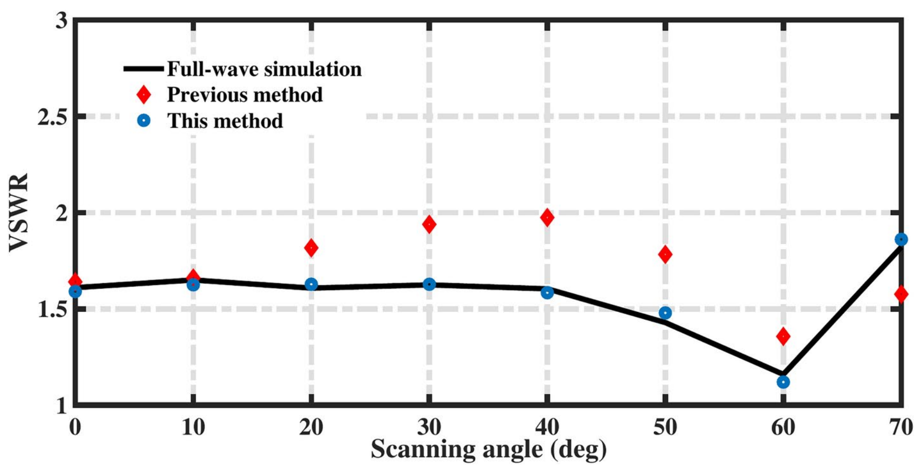

Fig. 13. Accuracy comparison of this method with previous one[22] for various scanning direction at H-plane.

highlights the effectiveness of the proposed matching structure in significantly improving the radiation performance of the circular waveguide array.

Discussion
Time and hardware reduction
One of the main advantages of the proposed methodology is its reduced computation time compared to traditional approaches that rely on full-wave simulations of the entire structure. Table 8 compares the required time and hardware usage for both design approaches. Moreover, to highlight the advantage of using surrogate models over numerical codes in WAIM evaluation, the expected time of the method in Ref.[23] is also included in Table 7. For all full-wave evaluations in this study, the FEM solver of ANSYS HFSS software is used on a PC with 32 GB RAM and a Core i7 CPU. To provide a sensible comparison of different approaches, we compare the time and resources spent to calculate the cascaded GSM for one scanning angle. Compared to the full-wave approach, the proposed method reduces the average evaluation time for a single scanning angle of the array from 10 min to 0.3 s. This significant improvement highlights the impracticality of relying on FEM full-wave simulation

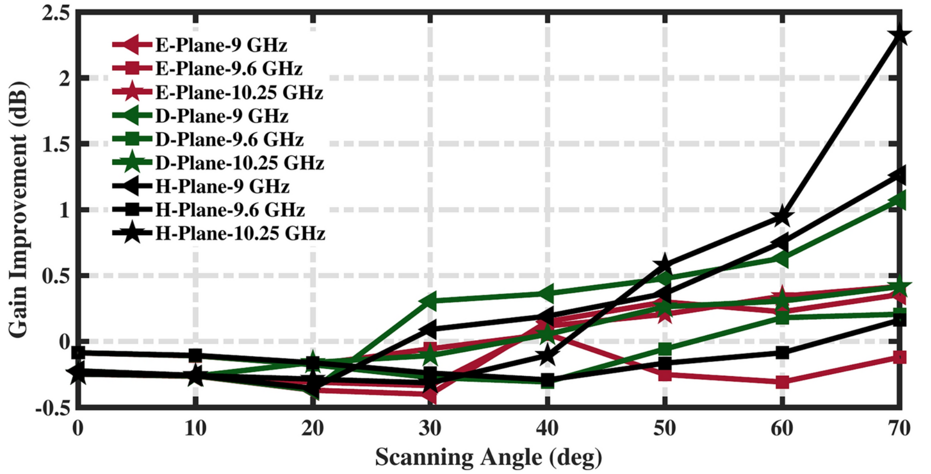

Fig. 14. Relative gain improvement of the array by adding WAIM.

Ref. No.	Max. Scanning angle (°)			Bandwidth (%)	Gain improvement at extreme scanning angle (dB)		
	E	D	H		E	D	H
Reference[20]	45	81	65	10	NA	NA	NA
Reference[13]	70	NA	70	13	NA	NA	NA
Reference[23]	70	70	70	6	0	− 0.25	∼ 0.6
This work	77	75	70	13	∼ 0.5	∼ 1	∼ 2

Table 5. Performance comparison with other works.

to optimize WAIM for array structures, requiring evaluation for several scanning angles and optimization generations. Compared to Ref.[23], our method reduces the calculation time for a single scanning angle by 500% while maintaining a generalized design approach. This indicates that, unlike Ref.[23], this method is much faster than conventional numerical codes, and more importantly, it does not require any specialized expertise to adapt to the new WAIM configurations. It only requires data preparation and model training. Moreover, the trained SM using DT requires minimal datasets, saving the data preparation time for new configurations. Table 9 provides a detailed computational cost breakdown for each step of this methodology. Preparing 200 datasets takes around 20 h, and training the ML models and selecting the best SM takes around 30 min. Once the SM is trained, it needs 0.3 s to evaluate the WAIM behavior at each scanning angle. A single generation of the optimization, including the WAIM evaluation at 24 angles and calculation of the GSMs, requires 9.6 s. Considering the 350 generations, for the first example, to find the optimal solution, our method can design the matching structure in 56 min. As illustrated in the examples, this method can be applied to other types of arrays as well. Depending on the complexity of the array and the WAIM structure, the required time for array evaluation and dataset preparation may vary. However, the GSM evaluation time for a single scanning angle—which is the key factor in determining the overall optimization time—will not change significantly.

In terms of computational resources, our method requires 9.7 MB for the optimization and GSM calculations, while the approach in Ref.[23] and full wave calculation need 43 MB and 18.2 GB, respectively. The key to this achievement is that our methodology eliminates the evaluation of the underlying array in each generation of the optimization process. Moreover, it uses a well-trained ML model to avoid resource-consuming EM calculations in predicting the WAIM characteristics. On the other hand, including the middle layer in the modeling has a negligible impact on the overall design time. Our method can evaluate the optimal parameters for the middle layer to achieve the best input impedance in a fraction of a second. This is a significant advantage compared to the traditional full-wave simulation methods, which require analyzing the whole structure for different values of the gap layer's parameters, including the dielectric constant and height. This process adds significantly to the design time, which is not included in the overall time of full-wave design.

Sensitivity analysis

Another aspect of the design that should be thoroughly studied is the sensitivity of different parameters. This assessment provides insights on the variables and their variations that significantly impact the array performance. In this regard, this information is particularly valuable from the fabrication perspective. To add this to our design, a sensitivity analysis is carried out by evaluating the importance of different features of the machine learning model trained for the WAIM, illustrated in Fig. 22. In this analysis, each feature is assigned a score based on its

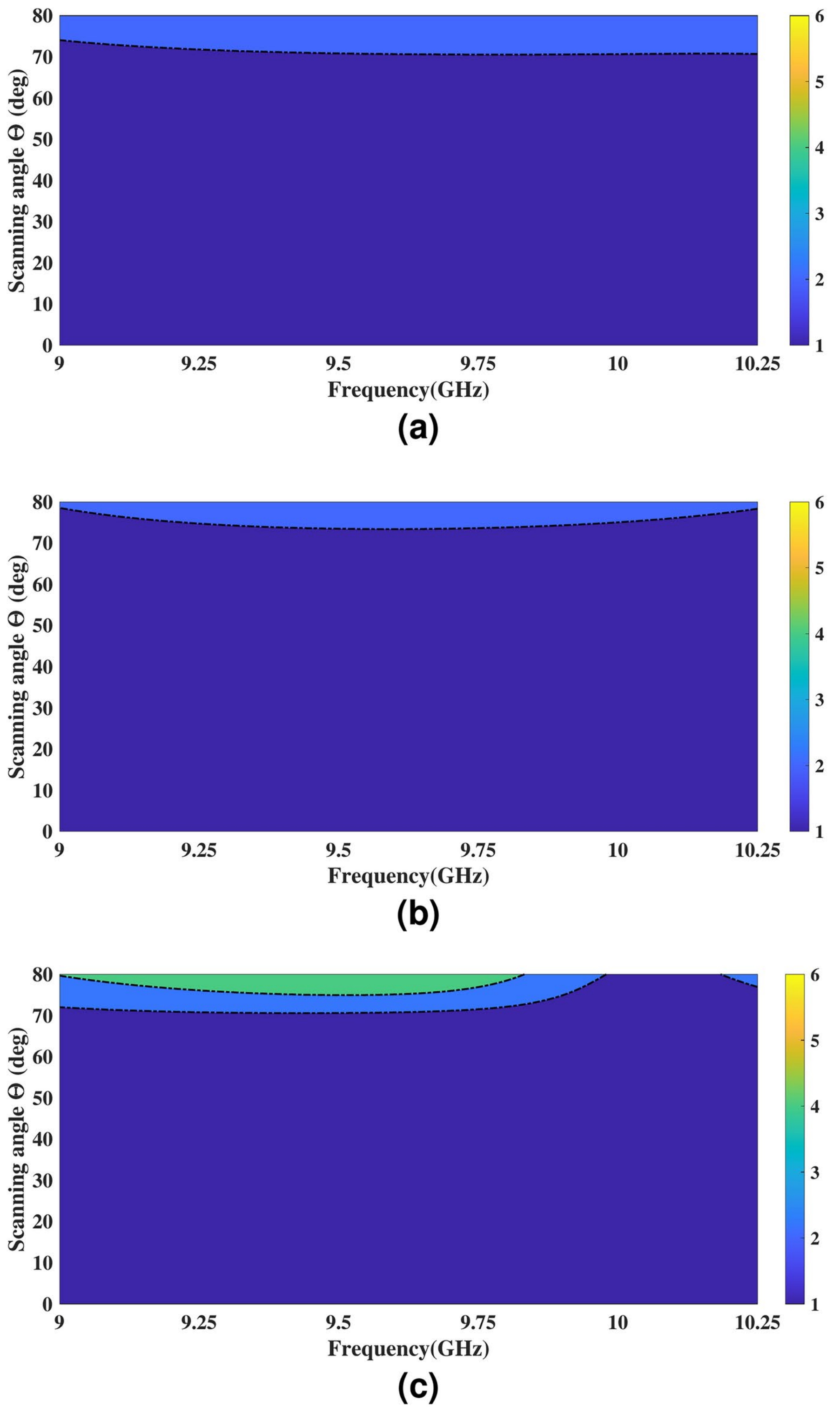

Fig. 15. VSWR results of full-wave simulation of the designed array by considering a dielectric in the intermediate layer (**a**) E-plane, (**b**) D-plane, (**c**) H-plane. First contour shows VSWR less than 2.

impact on the model's output. The score is determined by introducing variations to a single feature and keeping all other features constant, allowing us to calculate the sensitivity of the model to changes in each parameter.

As demonstrated, besides the scanning angles which have significant effects on the outcome of the trained model, among the structural parameters the width of both strips, w_x and w_y, have the most impact on the final results. After that, we should be careful about parameters such as h_x, l_x, l_y. These findings suggest that careful attention should be given to the precise fabrication of the strip widths, as small variations in these parameters can

Variable	Value	Variable	Value	Variable	Value	Variable	Value
w_x	2.9	g_x	1.8	l_x	7	h_x	5.4
w_y	4.1	g_y	1.9	l_y	3.7	d	4

Table 6. Dimensions of the designed loaded array.

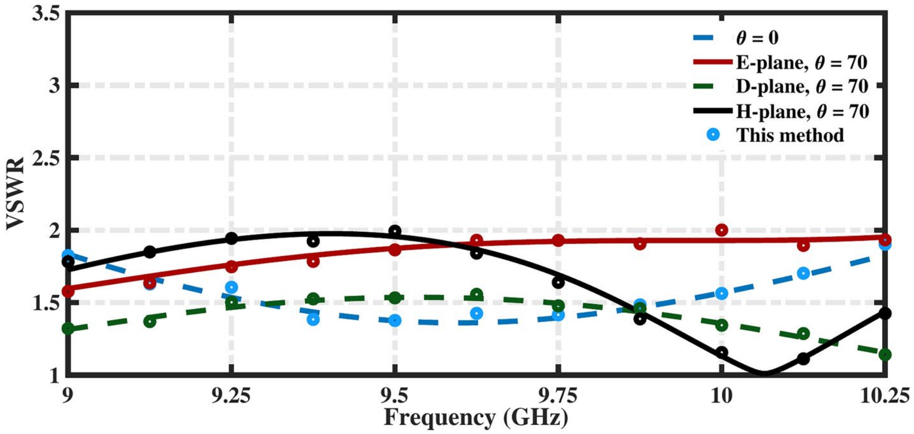

Fig. 16. Comparison between the outcome of proposed method and HFSS simulation results.

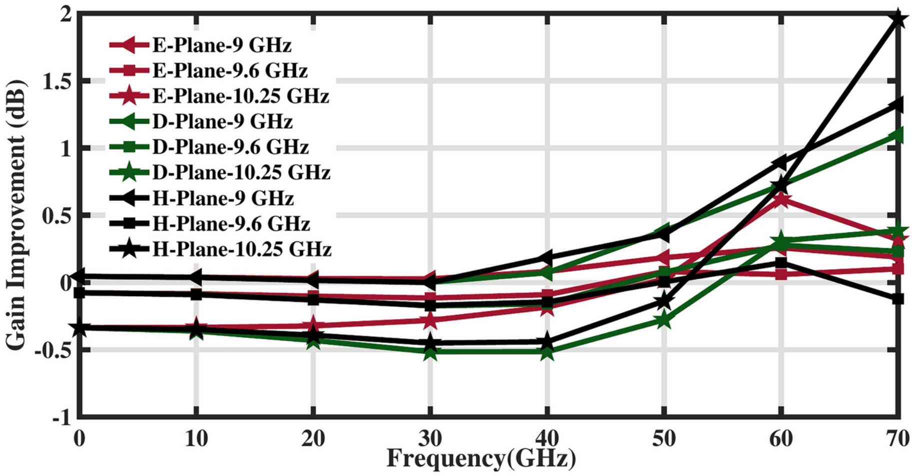

Fig. 17. Relative gain improvement of the array by adding WAIM.

lead to considerable discrepancies from the desired results. By prioritizing these key parameters, the proposed design can achieve reliable performance by reducing fabrication-induced errors.

Conclusion

The proposed methodology provides an efficient approach to designing WAIM structures to improve the scanning range of arbitrary arrays. The Floquet modal expansion and GSM analysis were employed to model the multi-layer structure, enabling the calculation of overall input impedance using the GSM of the three layers, regardless of their shapes. Additionally, integrating a decision-tree-based ML model significantly reduces computational cost and eliminates the need for human expertise in numerical code development to analyze the WAIM structures. The methodology considered sufficient excited harmonics incorporated all modal interactions within the WAIM structure. It utilized an accurate SM by evaluating different ML models, enhancing the overall accuracy. Through the GA optimization procedure, this method effectively achieved an optimal structure to improve the array's scanning range. Unlike the previous approaches, this model can evaluate the array performance for different materials utilized to fill the gap layer, not just air. This capacity is essential as it considers the effects of the matching layer's supporting structure, increasing accuracy from a fabrication perspective. The verification through three different array configurations demonstrates the versatility

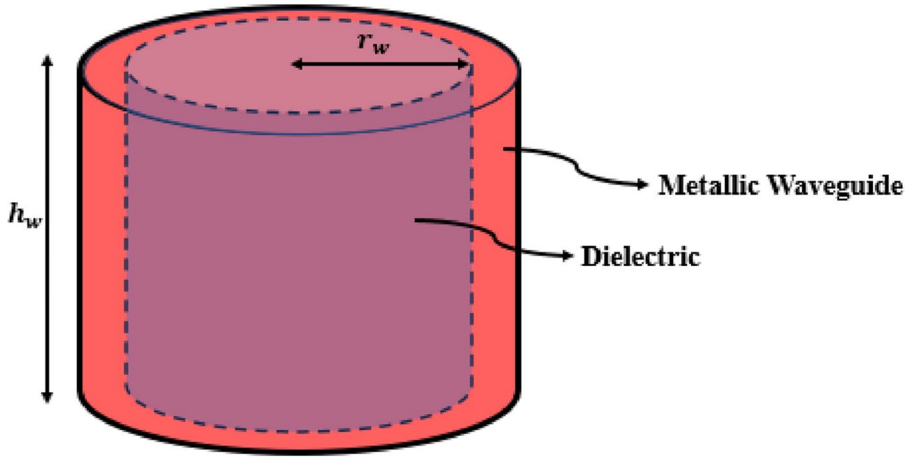

Fig. 18. Metallic waveguide filled with dielectric as the array element with $r_w = 6.2\,\mathrm{mm}$ and $h_w = 25\,\mathrm{mm}$.

and effectiveness of the proposed framework. Compared to the previous approaches, the proposed method significantly reduces computational time and resources, offering a low-cost, feasible solution. This methodology establishes a robust foundation for developing advanced tools to design wide-angle scanning arrays.

Despite these advantages, some limitations should be acknowledged. While the proposed WAIM structure exhibits flexibility and has been successfully applied to multiple array configurations, certain array structures may require alternative WAIM designs to achieve optimal performance. Future research could explore the development of a more universal WAIM configuration that can be applied to a broader range of array architectures. Additionally, while this work establishes a robust numerical and ML-driven framework, further validation through physical prototyping and experimental measurements is necessary to confirm the practical feasibility of the designed WAIM structures.

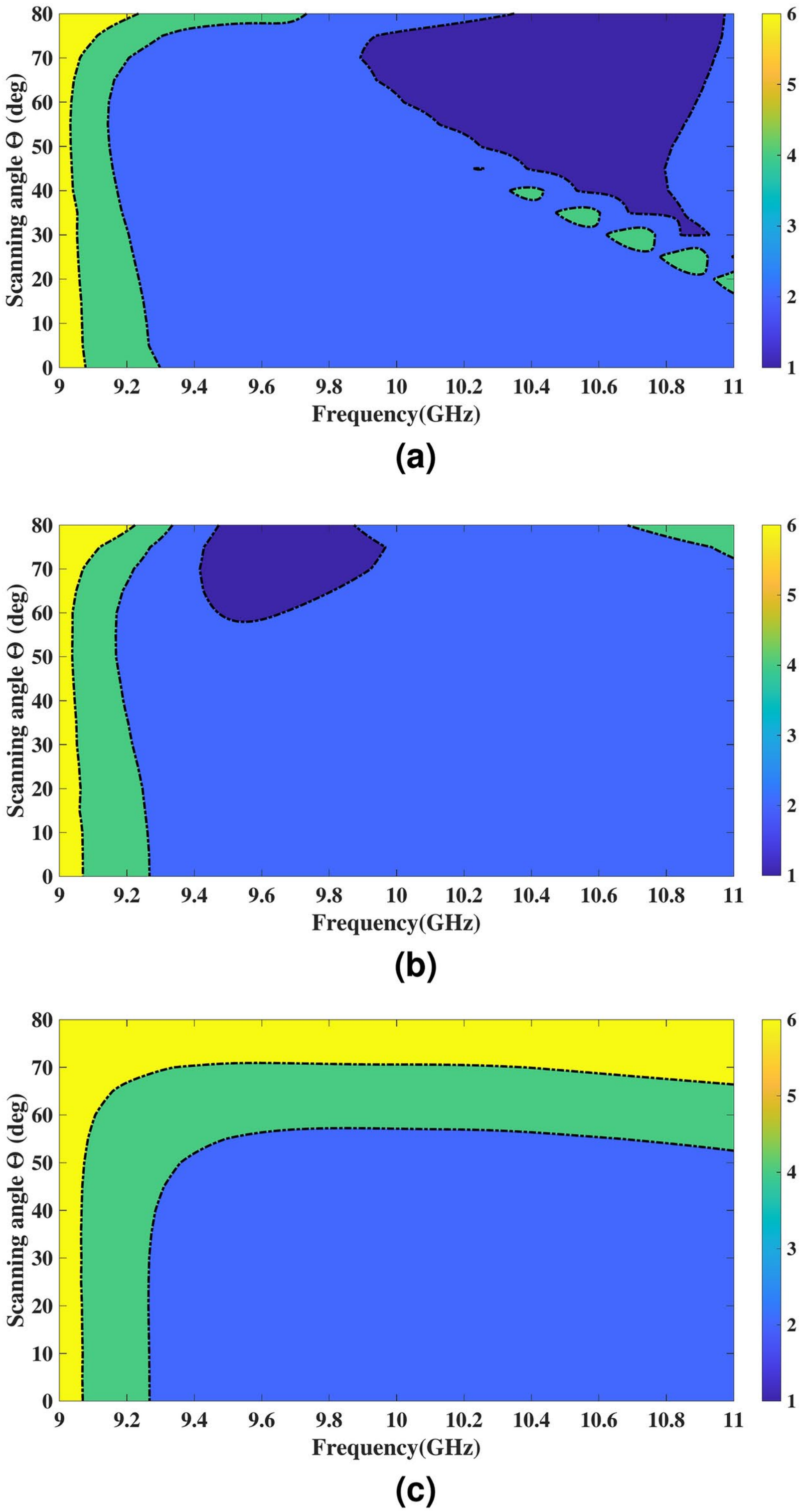

Fig. 19. VSWR results of full-wave simulation of the waveguide array without WAIM at (**a**) E-plane, (**b**) D-plane, (**c**) H-plane.

Variable	Value	Variable	Value	Variable	Value	Variable	Value
w_x	4	g_x	2	l_x	4.5	h_x	0
w_y	2	g_y	0.8	l_y	4	d	3

Table 7. Dimensions of the designed matching configuration for waveguide array.

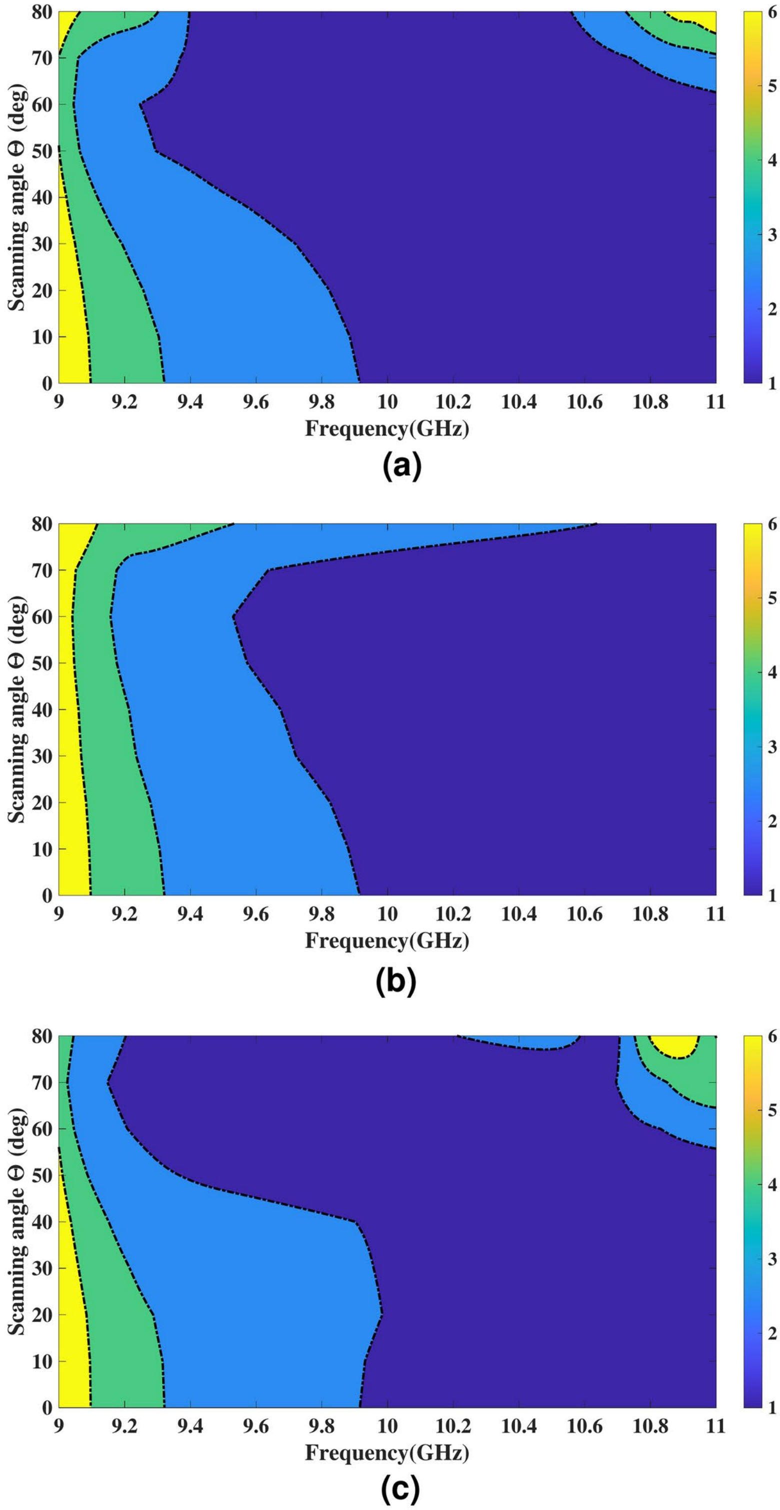

Fig. 20. VSWR results of full-wave simulation of the loaded waveguide array at (**a**) E-plane, (**b**) D-plane, (**c**) H-plane.

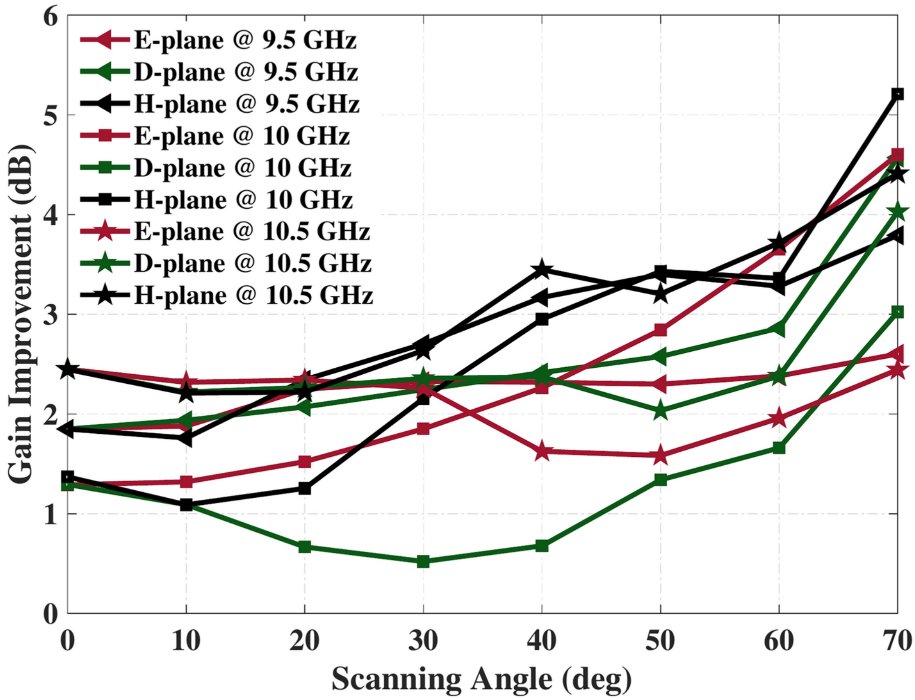

Fig. 21. Relative gain improvement of the waveguide array by adding the WAIM.

	This method	Reference[23]	Full wave
GSM evaluation for a single scanning angle	0.3 s	1.2 s	10 min 15 s
RAM usage (peak)	9.7 MB	43 MB	18.2 GB

Table 8. Time and resource comparison of three approaches for designing loaded array.

	This method	Full wave
Dataset preparation time	20 h	–
ML training time	29 min 23 s	–
GSM evaluation time for a single scanning angle	0.3 s	10 min 15 s
GSM evaluation time for all directions	9.6 s	4 h 6 min
Design time	56 min	1435 h

Table 9. Computational cost breakdown comparing this method and the full-wave approach.

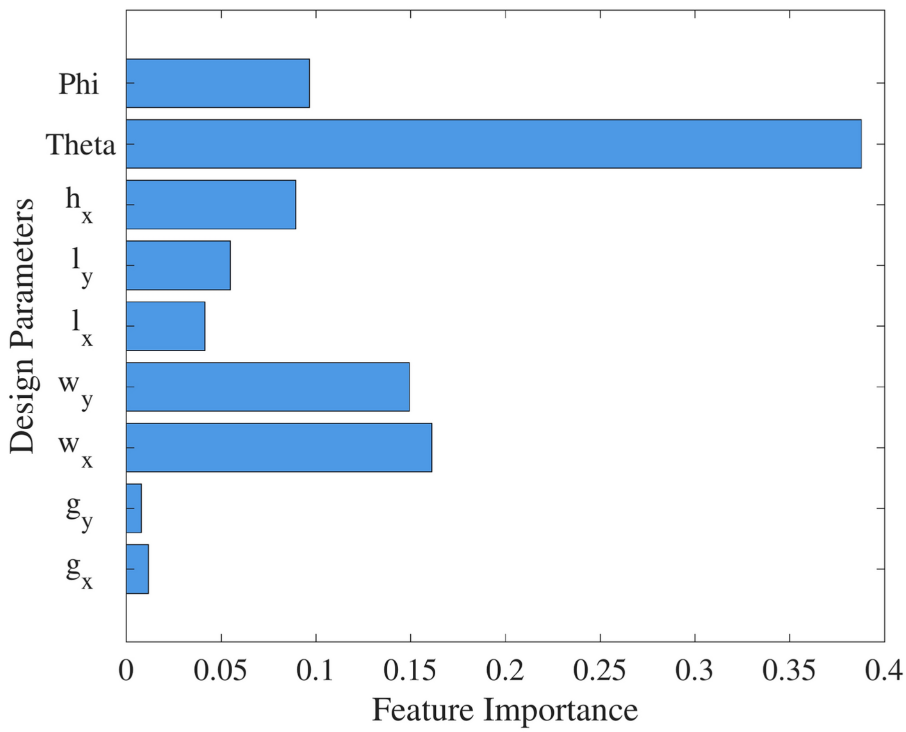

Fig. 22. Sensitivity analysis on the WAIM parameters.

Data availability

All data generated or analyzed during this study are included in this published article. For any further data, you can contact the corresponding author, Sina Hasibi Taheri (sina.hasibitaheri@mq.edu.au)

Received: 4 February 2025; Accepted: 28 April 2025
Published online: 13 May 2025

References

1. Bhattacharyya, A. K. *Phased Array Antennas: Floquet Analysis, Synthesis, BFNs and Active Array Systems* Vol. 179 (Wiley, Hoboken, 2006).
2. Hansen, R. C. *Phased Array Antennas* (Wiley, Hoboken, 2009).
3. Pozar, D. & Schaubert, D. Scan blindness in infinite phased arrays of printed dipoles. *IEEE Trans. Antennas Propag.* **32**, 602–610 (1984).
4. Edelberg, S. & Oliner, A. Mutual coupling effects in large antenna arrays: Part 1-slot arrays. *IRE Trans. Antennas Propag.* **8**, 286–297 (1960).
5. Hannan, P., Lerner, D. & Knittel, G. Impedance matching a phased-array antenna over wide scan angles by connecting circuits. *IEEE Trans. Antennas Propag.* **13**, 28–34 (1965).
6. Xia, R.-L. et al. Wide-angle scanning phased array using an efficient decoupling network. *IEEE Trans. Antennas Propag.* **63**, 5161–5165 (2015).
7. Yang, G. & Zhang, S. Dual-polarized wide-angle scanning phased array antenna for 5G communication systems. *IEEE Trans. Antennas Propag.* **70**, 7427–7438 (2022).
8. Su, Z.-L., Leung, K. W. & Lu, K. A shaped-beam antenna for wide-angle scanning phased array. *IEEE Trans. Antennas Propag.* **70**, 7659–7669 (2022).
9. Arand, B. A., Bazrkar, A. & Zahedi, A. Design of a phased array in triangular grid with an efficient matching network and reduced mutual coupling for wide-angle scanning. *IEEE Trans. Antennas Propag.* **65**, 2983–2991 (2017).
10. Yang, G., Li, J., Wei, D. & Xu, R. Study on wide-angle scanning linear phased array antenna. *IEEE Trans. Antennas Propag.* **66**, 450–455 (2017).
11. Magill, E. & Wheeler, H. Wide-angle impedance matching of a planar array antenna by a dielectric sheet. *IEEE Trans. Antennas Propag.* **14**, 49–53 (1966).
12. Lee, S. & Mittra, R. Radiation from dielectric-loaded arrays of parallel-plate waveguides. *IEEE Trans. Antennas Propag.* **16**, 513–519 (1968).
13. Yun, J., Park, D., Jang, D. & Hwang, K. C. Design of an active beam-steering array with a perforated wide-angle impedance matching layer. *IEEE Trans. Antennas Propag.* **69**, 6028–6033 (2021).
14. Sajuyigbe, S. et al. Wide angle impedance matching metamaterials for waveguide-fed phased-array antennas. *IET Microwav. Antennas Propag.* **4**, 1063–1072 (2010).
15. Manica, L., Carlin, M., Malcic, I., Oliveri, G. & Massa, A. Wideband multilayer Waim design and optimization. In *The 8th European Conference on Antennas and Propagation (EuCAP 2014)*, 2997–3000 (IEEE, 2014).
16. Silvestri, F., Chiusolo, P., Cifola, L., Bolt, R. & Gerini, G. Design of metamaterial based wide angle impedance matching layers for active phased arrays. In *2015 9th European Conference on Antennas and Propagation (EuCAP)* 1–5 (IEEE, 2015).
17. Bah, A. O., Qin, P.-Y., Ziolkowski, R. W., Cheng, Q. & Guo, Y. J. Realization of an ultra-thin metasurface to facilitate wide bandwidth, wide angle beam scanning. *Sci. Rep.* **8**, 4761 (2018).

18. Hu, C.-H. et al. Conjugate impedance matching method for wideband and wide-angle impedance matching layer with 70° scanning in the h-plane. *IEEE Antennas Wirel. Propag. Lett.* **20**, 63–67 (2020).
19. Jin, F.-L., Ding, X., Cheng, Y.-F., Wang, B.-Z. & Shao, W. Impedance matching design of a low-profile wide-angle scanning phased array. *IEEE Trans. Antennas Propag.* **67**, 6401–6409 (2019).
20. Cameron, T. R. & Eleftheriades, G. V. Analysis and characterization of a wide-angle impedance matching metasurface for dipole phased arrays. *IEEE Trans. Antennas Propag.* **63**, 3928–3938 (2015).
21. Oliveri, G., Salucci, M., Anselmi, N. & Massa, A. Multiscale system-by-design synthesis of printed WAIMs for waveguide array enhancement. *IEEE J. Multiscale Multiphys. Comput. Tech.* **2**, 84–96 (2017).
22. Silvestri, F., Cifola, L. & Gerini, G. Diamagneto-dielectric anisotropic wide angle impedance matching layers for active phased arrays. *Prog. Electromagn. Res. B* **70**, 1–12 (2016).
23. Bianchi, D., Genovesi, S., Borgese, M., Costa, F. & Monorchio, A. Element-independent design of wide-angle impedance matching radomes by using the generalized scattering matrix approach. *IEEE Trans. Antennas Propag.* **66**, 4708–4718 (2018).
24. Zhang, J., Xu, J., Chen, Q. & Li, H. Machine-learning-assisted antenna optimization with data augmentation. *IEEE Antennas Wirel. Propag. Lett.* **22**, 1932–1936 (2023).
25. Pavithran, S., Viswasom, S., Asha, J. *et al.* Designing of a 5G multiband antenna using decision tree and random forest regression models. In *2021 8th International Conference on Signal Processing and Integrated Networks (SPIN)* 626–631 (IEEE, 2021).
26. Shi, D., Lian, C., Cui, K., Chen, Y. & Liu, X. An intelligent antenna synthesis method based on machine learning. *IEEE Trans. Antennas Propag.* **70**, 4965–4976 (2022).
27. Gong, Z., Ding, Y., Chen, Y. & Cree, M. J. Wearable microwave medical sensing for stroke classification and localization: A space-division-based decision-tree learning method. *IEEE Trans. Antennas Propag.* **71**, 6906–6917 (2023).
28. Wang, P. et al. A machine learning framework for the design of STCDME structures in RIS applications. *IEEE Trans. Microw. Theory Tech.* **72**, 1467–1479 (2023).
29. Feng, N. *et al.* Gradient boosting decision tree based PMM model integrated into FDTD method for solving subsurface sensing problems. *IEEE Trans. Antennas Propag.* (2024).
30. Zhao, Y. et al. Reconstruction of the statistical characteristics of electric fields in enclosures with an aperture based on random forest regression. *IEEE Trans. Electromagn. Compat.* **62**, 1151–1159 (2019).
31. Zhang, L., Ni, Q., Zhai, M., Moreno, J. & Briso, C. An ensemble learning scheme for indoor-outdoor classification based on KPIS of LTE network. *IEEE Access* **7**, 63057–63065 (2019).
32. Sharma, Y., Zhang, H. H. & Xin, H. Machine learning techniques for optimizing design of double t-shaped monopole antenna. *IEEE Trans. Antennas Propag.* **68**, 5658–5663 (2020).
33. Cui, L., Zhang, Y., Zhang, R. & Liu, Q. H. A modified efficient KNN method for antenna optimization and design. *IEEE Trans. Antennas Propag.* **68**, 6858–6866 (2020).
34. Wu, Q., Chen, W., Yu, C., Wang, H. & Hong, W. Machine learning-assisted optimization for antenna geometry design. *IEEE Trans. Antennas Propag.* (2024).
35. Jiao, Y., Zhu, Q., Ni, R. & Cheng, Q. S. A multisurrogate-assisted optimization framework for SSPP-based mmWave array antenna. *IEEE Trans. Antennas Propag.* **71**, 2938–2945 (2023).
36. Akhlaghi, B. et al. Predictive deep learning for pitting corrosion modeling in buried transmission pipelines. *Process Saf. Environ. Prot.* **174**, 320–327 (2023).
37. Mesghali, H. et al. Predicting maximum pitting corrosion depth in buried transmission pipelines: Insights from tree-based machine learning and identification of influential factors. *Process Saf. Environ. Prot.* **187**, 1269–1285 (2024).
38. Houkan, A. *et al.* Enhancing security in industrial IoT networks: Machine learning solutions for feature selection and reduction. *IEEE Access* (2024).
39. Sharma, P. et al. Comprehensive study of spinel nanoparticles using experimental, theoretical and machine learning methods. *Physica B* **699**, 416820 (2025).
40. Costa, V. G. & Pedreira, C. E. Recent advances in decision trees: An updated survey. *Artif. Intell. Rev.* **56**, 4765–4800 (2023).
41. Koziel, S., Pietrenko-Dabrowska, A. & Leifsson, L. Antenna optimization using machine learning with reduced-dimensionality surrogates. *Sci. Rep.* **14**, 21567 (2024).
42. Monni, S., Gerini, G., Neto, A. & Tijhuis, A. G. Multimode equivalent networks for the design and analysis of frequency selective surfaces. *IEEE Trans. Antennas Propag.* **55**, 2824–2835 (2007).
43. Wan, C. & Encinar, J. A. Efficient computation of generalized scattering matrix for analyzing multilayered periodic structures. *IEEE Trans. Antennas Propag.* **43**, 1233–1242 (1995).
44. Bhattacharyaa, A. Analysis of multilayer infinite periodic array structures with different periodicities and axes orientations. *IEEE Trans. Antennas Propag.* **48**, 357–369 (2000).
45. Pozar, D. M. Microwave engineering. *Fourth Editions, University of Massachusetts at Amherst* 26–30 (Wiley, 2012).
46. Hanson, G. W. & Yakovlev, A. B. Investigation of mode interaction on planar dielectric waveguides with loss and gain. *Radio Sci.* **34**, 1349–1359 (1999).
47. Sun, B., Loison, R., Gillard, R., Estebe, É. & Renard, C. 3D wide-angle impedance matching for X-band phased array. In *2021 15th European Conference on Antennas and Propagation (EuCAP)* 1–5 (IEEE, 2021).

Acknowledgements
This work was supported in part by the Macquarie University International Research Stipend Program (RTP) Scholarship funded by the Commonwealth Government, Australia; in part by the Icelandic Research Fund under Grant 2410297; and in part by the National Science Centre of Poland under Grant 2020/37/B/ST7/01448.

Author contributions
S.H.T.—Background study, conceptualization, Coding, simulation, data analysis, manuscript writing, and editing; J.M: manuscript editing, coding, data analysis; A.L.—Supervision, technical suggestion, manuscript review; S.K.—Results analysis and review of the manuscript; S.S.- Results analysis, review of the manuscript and funding acquisition.

Declarations

Competing interests
The authors declare no competing interests.

Additional information
Correspondence and requests for materials should be addressed to S.H.T.

Reprints and permissions information is available at www.nature.com/reprints.